Computational Ghost Rotational Doppler Metrology

Fei Lin,[1] Ling Hong,[1] Yuan Ren,[2,*] Xiaodong Qiu⊙,[1,†] and Lixiang Chen[1,‡]

[1]*Department of Physics, Xiamen University, Xiamen 361005, China*

[2]*Department of Aerospace Science and Technology, Space Engineering University, Beijing 101416, China*

We present a scheme for measuring a rotational Doppler frequency shift with only a single-shot measurement. Our protocol benefits from the combination of computational temporal ghost imaging and heterodyne detection of the rotational Doppler effect. Specifically, by multiplexing a series of elaborately designed ring-shaped spatial patterns, we map the temporal rotational Doppler signal into the spatial domain and thus can collect the Doppler signal with a camera in a single-shot exposure. Then, by calculating intensity correlations between the resulting elaborate spatial patterns and the image captured by the camera, we reconstruct the temporal Doppler signal. In our experiments, we succeed in demonstrating fairly good performance for measuring the angular velocity of a real spinning object with a rough surface. Our scheme could find potential applications in remote sensing and could also inspire more attempts to develop protocols for temporal detection and processing on the basis of space-time duality.

I. INTRODUCTION

Similarly to the linear Doppler effect, describing the frequency shift of a wave reflected from a linearly moving object [1,2], a frequency shift is also encountered when a wave is reflected or emitted from a rotating object; this is termed the rotational Doppler effect [3–6]. This effect was observed by Garetz and Arnold, who successfully imprinted a frequency shift on circularly polarized light via a rotating half-wave plate [7]. In addition to its spin angular momentum, in 1992, Allen *et al.* demonstrated that a photon can also carry an orbital angular momentum (OAM) of $\ell\hbar$, which arises from a twisted phase wavefront described by $\exp(i\ell\varphi)$, where φ is the azimuthal angle and ℓ can be an arbitrary integer [8]. Subsequently, the rotational Doppler effect was demonstrated with millimeter waves carrying an OAM; interestingly enough, the value of the rotational Doppler frequency shift is directly proportional to the OAM [9], which implies that by using a higher OAM, one could amplify the frequency shift and thus measure it accurately [10]. Significantly, in 2013, Lavery *et al.* extended the rotational Doppler effect to visible light and experimentally measured the angular velocity of a spinning object using light scattered from its surface [3]. They demonstrated further that, unlike the linear Doppler shift, the rotational Doppler shift is achromatic, and even white light with an OAM can produce a single-valued

Doppler shift [11]. To further improve the applications of the rotational Doppler effect, researchers have enlarged the detection distance for the rotational Doppler effect from several meters in the laboratory to a 120-m free-space optical link in a realistic city environment [12]. Much attention has also been paid to analyzing the influence of compound motion of the object and the complex relative pose between the OAM beam and the object on the rotational Doppler signal [13–18]. Recently, the original linear-optics-based detection method for the rotational Doppler effect has been extended to nonlinear-optics-based detection, paving the way for high-efficiency infrared monitoring [19,20].

The rotational Doppler frequency shift is routinely detected by means of a beat-frequency signal produced by interference between superposed OAM beams [3], via which the optical high-frequency signal can be converted to a slowly time-varying intensity signal. We note that, in recent years, there has been increased interest in the space-time duality of electromagnetic waves, which has enabled significant advances in the detection and processing of time-varying signals, such as in ultrafast optical oscilloscopes [21], temporal cloaking [22], and all-optical correlations [23]. Particularly, by extending spatial-domain ghost imaging to the time domain, i.e., temporal ghost imaging, one can retrieve a temporal object with a slow detector in a nonlocal manner [24,25]. Because of this unique property, temporal ghost imaging has potential applications in the dynamic characterization of free-electron lasers [26], quantum secure communications [27,28], and quantum device evaluation [29]. The rotational Doppler frequency shift is generally revealed

———————
*renyuan_823@aliyun.com
†qxd@xmu.edu.cn
‡chenlx@xmu.edu.cn

by the time-varying beat-frequency signal, which can be fairly seen as a "time object". In this regard, whether or not temporal ghost imaging can be used to detect a rotational Doppler signal, and what new features this might lead to, forms the major incentive for our present work. In addition, previous schemes have focused only on the time variation of the rotational Doppler signal, whereas the spatial distribution of Doppler signals has not yet been fully explored [3,30].

Here, by multiplexing a series of elaborately designed ring-shaped spatial patterns, we map the temporal rotational Doppler signal into the spatial domain and thus are able to present a detection scheme that enables single-shot acquisition of the Doppler signal with a camera that has no temporal resolution. Our protocol can be seen as a combination of rotational Doppler detection and computational temporal ghost imaging, and thus is termed computational ghost rotational Doppler detection. In our experiments, we succeed in demonstrating fairly good performance of ghost rotational Doppler detection for a simple geometric object and, particularly, for a real object with a rough surface.

II. THEORETICAL ANALYSIS AND EXPERIMENTAL SCHEME

Theoretically, a rotating object $\psi(r, \varphi)$ can be expressed via a Fourier series expansion [31,32]

$$\psi(r, \varphi + \Omega t) = \sum_n A_n(r) \exp(in\varphi) \exp(in\Omega t), \quad (1)$$

where r and φ are the radial and the angular coordinate, respectively, $A_n(r)$ is the complex amplitude of the nth-order OAM mode, and Ω is the rotational angular velocity. From Eq. (1), one can see that each OAM component carries an OAM-related time-varying phase $\exp(in\Omega t)$; that is to say, it exhibits a frequency shift of $n\Omega$. To extract this frequency shift, one commonly adopts a specific superposition of OAM modes comprising two helical-phase beams with opposite values of ℓ, $\Phi(r, \varphi) = [\exp(i\ell\varphi) + \exp(-i\ell\varphi)]/\sqrt{2}$, to illuminate the rotating object, and thus the intensity of the scattered light can be expressed as

$$I(r, \varphi, t) = \left| \sum_m A_{m-\ell}(r) \exp(im\varphi) \exp[i(m-\ell)\Omega t] \right.$$
$$\left. + \sum_m A_{m+\ell}(r) \exp(im\varphi) \exp[i(m+\ell)\Omega t] \right|^2.$$
$$(2)$$

Routinely, the fundamental mode with $m = 0$ is then selected by a single-mode fiber, in which two different frequency components interfere with each other to produce a beat-frequency signal $I_{m=0} \propto \cos(2\ell\Omega t + \phi) + 1$,

where $\phi = \arg(A_{-\ell}A_\ell^*)$. Subsequently, this time-varying intensity signal is generally collected via a fast photodetector to allow one to conduct a Fourier time-frequency analysis to extract the frequency shift [3]. Compared with directly detecting the time-varying intensity signal, temporal ghost imaging looks attractive for dynamic imaging of waveforms with high resolution [24]. Particularly, computational temporal ghost imaging can realize single-shot acquisition of a nonreproducible time object via fully spatial multiplexing of the temporal intensity signal [25]. A critical precondition for using computational temporal ghost imaging is that points in the same transverse position in the time object possess the same variation tendency, i.e., the object is a one-dimensional time object. However, as shown in Eq. (2), the intensity of the scattered light varies in time and space, which indicates that the rotational Doppler signal is a more complex two-dimensional time object. In this regard, one question arises spontaneously: can we use temporal ghost imaging to detect the rotational Doppler signal?

In fact, the same beat-frequency Doppler signal occurs for high-order OAM modes, according to Eq. (2), and the different OAM modes generally have doughnut-shaped intensity distributions with different radii. Inspiringly, we could convert the rotational Doppler signal into a one-dimensional time object by conducting the integration in the azimuthal domain. With this consideration, Eq. (2) can be simplified to

$$I_h(r, t) = \int d\varphi\, I(r, \varphi, t)$$
$$= \sum_m |A_{m-\ell}(r)|^2 + \sum_m |A_{m+\ell}(r)|^2$$
$$+ \sum_m A_{m-\ell}(r) A_{m+\ell}^*(r) \exp(i2\ell\Omega t) + \text{c.c.}, \quad (3)$$

where $\sum_m |A_{m-\ell}(r)|^2 + \sum_m |A_{m+\ell}(r)|^2$ represents the direct-current signal, and the third term is the desired beat-frequency signal. Interestingly, the intensities of the light beams at different radii possess the same modulation frequency $f_m = |2\ell\Omega|/2\pi$. In other words, the rotational Doppler signal is a radial one-dimensional time object. Accordingly, we can conduct a computational ghost rotational Doppler measurement via ring-shaped spatial multiplexing. Our experimental setup is illustrated in Fig. 1(a). After being collimated and expanded, the beam from a 633-nm He-Ne laser is guided to illuminate a spatial light modulator (SLM) (Hamamatsu, X10468-01), which is used to display elaborate holographic gratings for producing the desired OAM superpositions with opposite signs of ℓ. The OAM superpositions encoded in the first-order diffracted beam are filtered out with an iris and then directed to illuminate the rotating object. Subsequently, the scattered light from the object, carrying the

rotational Doppler signal, is spatially sampled and multiplexed by passing it through a series of ring-shaped patterns, which are displayed in chronological order by a digital micromirror device (DMD) (Texas Instruments, V-7001). Finally, the ring-shaped patterns are imaged onto a CCD camera by a $4f$ imaging system consisting of two lenses ($f_3 = 300$ mm and $f_4 = 200$ mm). Here, the CCD camera plays the role of a non-time-resolved detector and collects all ring-shaped patterns in a single-shot exposure.

The key to our protocol is ring-shaped spatial multiplexing in the DMD plane, where the beat-frequency rotational Doppler signals at different times are mapped into corresponding ring-shaped patterns; this is similar to the concept of snapshot compressive-spectral imaging [33]. As shown in Fig. 1(b), we use the DMD to successively load the time-stamped ring-shaped patterns R_{t_i}, where the white regions are completely transparent and the black regions have zero transmission. Each pattern consists of several annuli, which are arranged on the basis of a Hadamard matrix, commonly used in single-pixel imaging [34]. In our experiments, the width of each annulus is roughly 41.1 μm . Specifically, the radial direction and the time series equivalently constitute a two-dimensional matrix, and each matrix element at the point (r_i, t_j) corresponds to an element of a Hadamard matrix. However, a Hadamard matrix is composed of 1s and −1s, whereas a DMD can display only 0s and 1s, corresponding to zero transmission and being completely transparent, respectively. In order to overcome this problem, we divide the Hadamard matrix H into two parts, a positive matrix H_+ and an inverted matrix H_-, which correspond to the positive and negative matrix elements, respectively. Accordingly, $H = H_+ - H_-$. In other words, we need to display two corresponding ring-shaped patterns $R_{t_i}^+$ and $R_{t_i}^-$ at each timestamp t_i via the DMD.

To acquire all time-stamped ring-shaped patterns in a single image, we set the exposure time of the CCD to 1 s and the switching time of the DMD to 31.25 ms. In this context, the beat-frequency rotational Doppler signal passing through the ring-shaped pattern at t_i can be expressed as

$$S_{t_i} = \iint_{r,\varphi} D \times \left(\frac{R_{t_i}^+}{C\left(R_{t_i}^+\right)} - \frac{R_{t_i}^-}{C\left(R_{t_i}^-\right)} \right), \qquad (4)$$

where D is the image recorded by the CCD camera, and $C(\cdot)$, the normalization coefficient, is equal to the area of the patterns. This is similar to the intensity-correlation operation in computational ghost imaging [25, 35]. Because the intensities of the light beams at different radii possess the same modulation frequency $2\ell\Omega$, as shown in Eq. (3), here S_t can represent the beat-frequency rotational Doppler signal. Similarly to conventional rotational Doppler detection, after performing a Fourier transformation of the temporal signals $\widetilde{I}(f) = \mathcal{F}(S_t)$, all the frequency components of the temporal signal can be obtained simultaneously.

III. RESULTS

In our first set of experiments, we use the SLM to simulate a rotating object in the form of a pentas flower [20]. By coding computer-generated holograms, we set the rotational angular velocity Ω of the pentas to 108 and 180 deg/s. Since the pentas has fivefold rotational symmetry, here, to enhance the signal, we use the OAM superpositions $\ell = \pm 5$ and $\ell = \pm 10$ to measure the rotational frequency shifts [3]. In addition, we adopt a 32-order Hadamard matrix as the sampling matrix. After spatial multiplexing, the beat-frequency Doppler signal is recorded by the CCD camera, as shown in the insets of
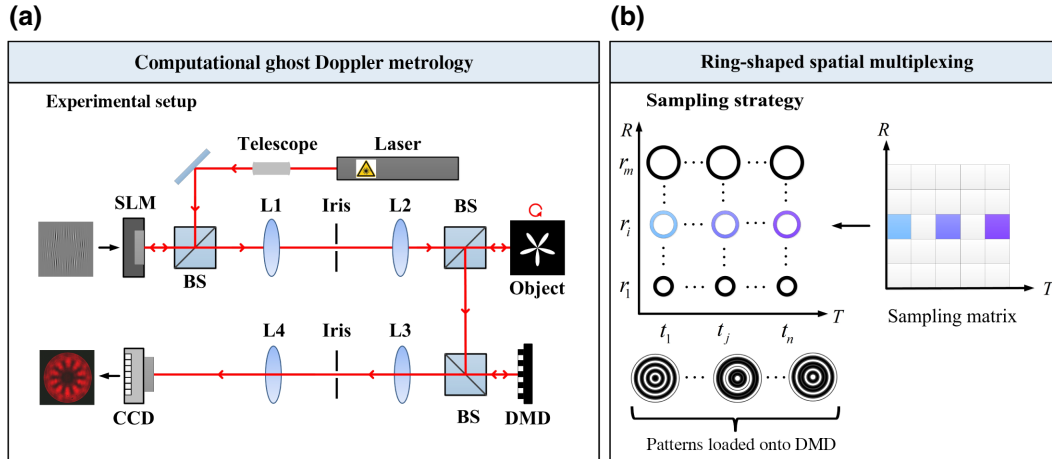

FIG. 1. Experimental scheme for computational ghost rotational Doppler metrology. (a) Schematic illustration of ghost Doppler metrology. BS, beam splitter. (b) Ring-shaped spatial multiplexing.
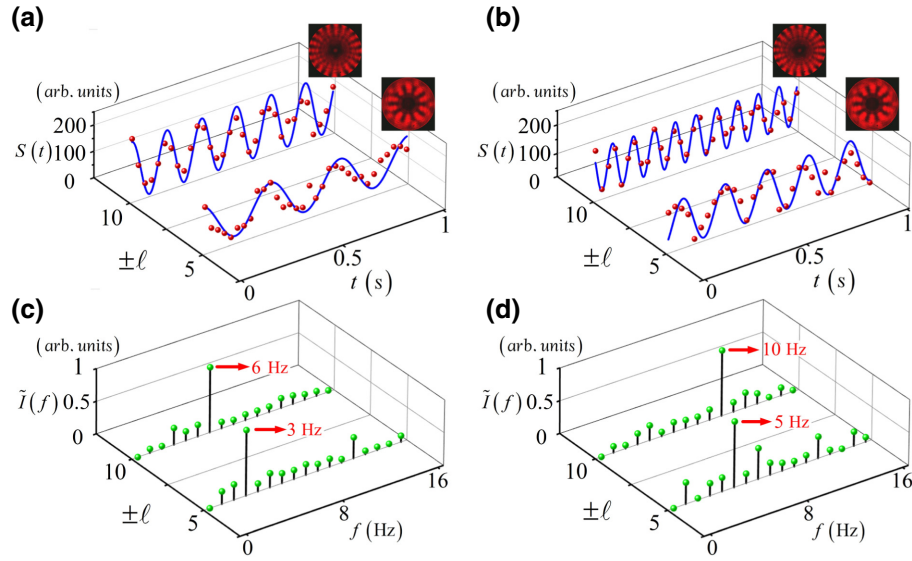
FIG. 2. Experimental results for a rotating pentas. (a),(b) Reconstructed temporal Doppler beat-frequency signals (the blue lines are fitted curves), where the rotational speed Ω of the object is 108 and 180 deg/s, respectively. The insets here show single-shot measurements recorded by the CCD camera. (c),(d) Corresponding power spectra of rotational Doppler signals, in which the beat frequencies are marked as well.

Figs. 2(a) and 2(b). By calculating intensity correlations between the time-stamped spatial patterns and the image captured by the CCD camera, as indicated by Eq. (4), we reconstruct the temporal beat-frequency Doppler signals, and we illustrate them in Figs. 2(a) and 2(b). From these, the cosine oscillations of the light intensities can be seen clearly. Then, as shown in Figs. 2(c) and 2(d), we perform a straightforward Fourier transformation on the temporal signals, and the corresponding power spectra of the Doppler signals are acquired. In Fig. 2(c), it is observed that there exist clearly distinguishable peaks at a frequency of 3 Hz for illumination with $\ell = \pm 5$, and at 6 Hz for the case of $\ell = \pm 10$. Then, according to the relation $f_m = |2\ell\Omega|/2\pi$, we deduce a rotational velocity $\Omega = 108$ deg/s, which is in good agreement with the theoretical value. In Fig. 2(d), we observe $f = 5$ Hz for $\ell = \pm 5$ and $f = 10$ Hz for $\ell = \pm 10$ and we deduce a rotational velocity $\Omega = 180$ deg/s, which is also consistent with the value that was set, thus demonstrating that our device is capable of reconstructing a temporal Doppler shift via a single-shot measurement. Here, we use the frequency crosstalk $P = \tilde{I}(f_m)/\sum_f \tilde{I}(f)$ to quantitatively evaluate the signal quality [36], where f_m corresponds to the rotational frequency of the object, namely $f_m = |2\ell\Omega|/2\pi$. Accordingly, the average crosstalk is about 0.3355. Note that, as shown in Figs. 2(c) and 2(d), there also exist some confused peaks at other frequencies, which arise mainly from the mode-spreading effect caused by the slight misalignment between the object's rotation axis and the center of the ring-shaped pattern loaded onto the DMD [37].

From a practical point of view, the objects to be detected usually have no obvious symmetry. To deal with this, we simulate a real object here with a rough glass surface, which is attached to a rotating rotor (illustrated in the inset of Fig. 3). In our experiments, the rotor is set to rotate successively at angular velocities $\Omega = 180, 360, 540, 720$, and 1080 deg/s. We acquire the corresponding power spectra of the Doppler signals via single-shot measurements similarly to what is done above. For the OAM superposition $\ell = \pm 1$ in Fig. 3(a), there are clearly discernible peaks at frequencies of 1, 2, 3, 4, and 6 Hz, which are directly proportional to the rotational velocities in accordance with $f = |2\ell\Omega|/2\pi$. Also, we use $\ell = \pm 2$ to illuminate the real object, and the experimental results are shown in Fig. 3(b). It is obvious that the peak frequency for the illumination with $\ell = \pm 2$ is twice that for $\ell = \pm 1$ at the same angular velocity. The average crosstalk is about 0.3980. The experimental results are consistent with the theoretical predictions and thus again confirm the effectiveness of our protocol.

IV. DISCUSSION

Theoretically, there are three main limiting factors affecting the quality of the signal. The first one arises from the mode-spreading effect [3,12,37] caused by the slight misalignment between the object's rotation axis and the center of the ring-shaped pattern loaded onto the DMD. The second factor is the imperfect imaging relationship between the DMD and the CCD camera. Computational ghost rotational Doppler metrology requires the operation of calculating an intensity correlation between the ring-shaped spatial patterns loaded onto the DMD and the
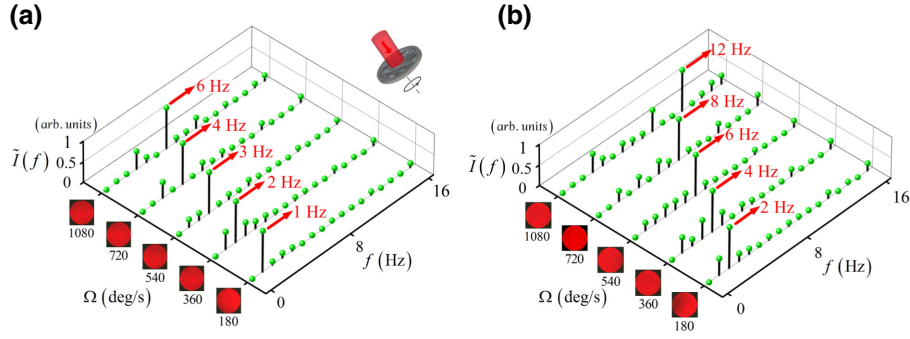
FIG. 3.   Experimental results for a rough glass surface. Illumination with the OAM superpositions (a) $\ell = \pm1$ and (b) $\ell = \pm2$.

image captured by the CCD camera. Consequently, imperfect imaging will introduce crosstalk between adjacent rings, and thus reconstruction errors arise. The third factor is the discretization of the Doppler signal arising from discontinuous rotation via loading the hologram grating onto the spatial light modulator to simulate the rotating object. Because the discretization is limited by the refresh rate of the SLM (typically 60 Hz), objects with a higher rotational speed are discretized more dramatically. In general, the discretization of a signal may result in energy leaking into other harmonic components [38], and thus degrade the signal quality.

Based on the principle of the discrete Fourier transform [38], the frequency resolution Δv is given by $\Delta v = f_s/N$, where N is the length of the signal. The sampling frequency f_s can be expressed as $f_s = N/T$, where T is the sampling time, i.e., the exposure time of the CCD camera. Accordingly, the frequency resolution is given by $\Delta v = 1/T$. In other words, the frequency resolution is determined by the sampling time. In our experiments, the maximum exposure time of our camera (Thorlabs, DCU224C) is 1.33 s, which implies that we can achieve only hertz-level frequency resolution. By using a camera with a longer exposure time, one could achieve millihertz resolution. We leave this possibility for our future studies. Furthermore, based on the principle of the Nyquist-Shannon sampling theorem, the measurable frequency bandwidth is given by $0 \leq f \leq (N/2)\Delta v$. In our system, N is the number of ring-shaped spatial patterns displayed via the DMD. Specifically, the DMD (Texas Instruments, V-7001), with a resolution of 1024×768 pixels, is used to perform the sampling and multiplexing tasks, and allows sampling of a maximum of 256 rings (with a radius of 3 pixels). As aforementioned, due to the fact that the DMD can display only 0s and 1s, corresponding to zero transmission and being completely transparent, respectively, we divide the Hadamard matrix H into two parts, a positive matrix H_+ and an inverted matrix H_-, which correspond to the positive and negative matrix elements, respectively. In this case, the maximum number of samples is $N_{\max} = 128$. As we know, the refresh rate of current commercial DMDs

is at the kilohertz level, that is to say, we can realize complete sampling on a millisecond scale, and so the achievable maximum frequency bandwidth can reach up to the kilohertz level.

V. CONCLUSION

In conclusion, we present a protocol for rotational Doppler metrology with only a single image in the spatial domain. Based on computational temporal ghost imaging and ring-shaped spatial multiplexing, we map the temporal rotational Doppler beat-frequency signal into the spatial domain. Then, similarly to computational ghost imaging or single-pixel imaging [39–41], we reconstruct the temporal beat-frequency Doppler signal via intensity correlations between time-stamped spatial patterns (the sample matrix) and the image captured by the CCD camera (the corresponding weight coefficients). In our experiments, we succeed in demonstrating fairly good performance of ghost rotational Doppler detection for a simple geometric object (a pentas flower) and, particularly, for a real object (a rough glass surface). Our scheme enables the detection of rotational speed without using a time-resolved detector and can be regarded as an important supplement to the conventional Doppler detection scheme. It may also inspire more attempts to develop protocols for temporal detection and processing on the basis of space-time duality [23].

[1] R. M. Measures, *Laser Remote Sensing, Fundamentals and Applications* (John Wiley and Sons, New York, 1984).

[2] H. S. Zapolsky, Doppler interpretation of quasar red shifts, Science **153**, 635 (1966).

[3] M. P. J. Lavery, F. C. Speirits, S. M. Barnett, and M. J. Padgett, Detection of a spinning object using light's orbital angular momentum, Science **341**, 537 (2013).

[4] M. Seghilani, M. Myara, I. Sagnes, B. Chomet, R. Bendoula, and A. Garnache, Self-mixing in low-noise semiconductor vortex laser: Detection of a rotational Doppler shift in backscattered light, Opt. Lett. **40**, 5778 (2015).

[5] L. Fang, Z. Y. Wan, A. Forbes, and J. Wang, Vectorial Doppler metrology, Nat. Commun. **12**, 4186 (2021).

[6] S. Qiu, T. Liu, Y. Ding, Z. Liu, L. Chen, and Y. Ren, Rotational Doppler effect with vortex beams: Fundamental mechanism and technical progress, Front. Phys. **10**, 938593 (2022).

[7] B. A. Garetz and S. Arnold, Variable frequency shifting of circularly polarized laser radiation via a rotating half-wave retardation plate, Opt. Commun. **31**, 1 (1979).

[8] L. Allen, M. W. Beijersbergen, R. J. C. Spreeuw, and J. P. Woerdman, Orbital angular momentum of light and the transformation of Laguerre-Gaussian laser modes, Phys. Rev. A **45**, 8185 (1992).

[9] J. Courtial, K. Dholakia, D. A. Robertson, L. Allen, and M. J. Padgett, Measurement of the Rotational Frequency Shift Imparted to a Rotating Light Beam Possessing Orbital Angular Momentum, Phys. Rev. Lett. **80**, 3217 (1998).

[10] J. Courtial, D. A. Robertson, K. Dholakia, L. Allen, and M. J. Padgett, Rotational Frequency Shift of a Light Beam, Phys. Rev. Lett. **81**, 4828 (1998).

[11] M. P. J. Lavery, S. M. Barnett, F. C. Speirits, and M. J. Padgett, Observation of the rotational Doppler shift of a white-light, orbital-angular-momentum-carrying beam backscattered from a rotating body, Optica **1**, 1 (2014).

[12] W. Zhang, J. Gao, D. Zhang, Y. He, T. Xu, R. Fickler, and L. Chen, Free-Space Remote Sensing of Rotation at the Photon-Counting Level, Phys. Rev. Appl. **10**, 044014 (2018).

[13] C. Rosales-Guzmán, N. Hermosa, A. Belmonte, and J. P. Torres, Direction-sensitive transverse velocity measurement by phase-modulated structured light beams, Opt. Lett. **39**, 5415 (2014).

[14] L. Fang, M. J. Padgett, and J. Wang, Sharing a common origin between the rotational and linear Doppler effects, Laser Photon. Rev. **11**, 1700183 (2017).

[15] X.-B. Hu, B. Zhao, Z.-H. Zhu, W. Gao, and C. Rosales-Guzmán, In situ detection of a cooperative target's longitudinal and angular speed using structured light, Opt. Lett. **44**, 3070 (2019).

[16] Y. Zhai, S. Fu, C. Yin, H. Zhou, and C. Gao, Detection of angular acceleration based on optical rotational Doppler effect, Opt. Express **27**, 15518 (2019).

[17] Y. Ren, S. Qiu, T. Liu, and Z. L. Liu, Compound motion detection based on OAM interferometry, Nanophotonics **11**, 1127 (2022).

[18] S. Qiu, Y. Ding, T. Liu, Z. Liu, and Y. Ren, Rotational object detection at noncoaxial light incidence based on the rotational Doppler effect, Opt. Express **30**, 20441 (2022).

[19] G. X. Li, T. Zentgraf, and S. Zhang, Rotational Doppler effect in nonlinear optics, Nat. Phys. **12**, 736 (2016).

[20] H. Guo, X. Qiu, S. Qiu, L. Hong, F. Lin, Y. Ren, and L. Chen, Frequency upconversion detection of rotational Doppler effect, Photon. Res. **10**, 183 (2022).

[21] M. A. Foster, R. Salem, D. F. Geraghty, A. C. Turner-Foster, M. Lipson, and A. L. Gaeta, Silicon-chip-based ultrafast optical oscilloscope, Nature **456**, 81 (2008).

[22] M. Fridman, A. Farsi, Y. Okawachi, and A. L. Gaeta, Demonstration of temporal cloaking, Nature **481**, 62 (2012).

[23] R. Salem, M. A. Foster, and A. L. Gaeta, Application of space–time duality to ultrahigh-speed optical signal processing, Adv. Opt. Photon. **5**, 274 (2013).

[24] P. Ryczkowski, M. Barbier, A. T. Friberg, J. M. Dudley, and G. Genty, Ghost imaging in the time domain, Nat. Photon. **10**, 167 (2016).

[25] F. Devaux, P.-A. Moreau, S. Denis, and E. Lantz, Computational temporal ghost imaging, Optica **3**, 698 (2016).

[26] D. Ratner, J. P. Cryan, T. J. Lane, S. Li, and G. Stupakov, Pump-Probe Ghost Imaging with SASE FELs, Phys. Rev. X **9**, 011045 (2019).

[27] S. Jiang, Y. R. Wang, T. Long, X. F. Meng, X. L. Yang, R. Shu, and B. Q. Sun, Information security scheme based on computational temporal ghost imaging, Sci. Rep. **7**, 7676 (2017).

[28] F.-X. Wang, J. Wu, W. Chen, S. Wang, D.-Y. He, Z. Q. Yin, C. L. Zou, G. C. Guo, and Z. F. Han, Perceiving Quantum Hacking for Quantum Key Distribution Using Temporal Ghost Imaging, Phys. Rev. Appl. **15**, 034051 (2021).

[29] J. Wu, F.-X. Wang, W. Chen, S. Wang, D.-Y. He, Z.-Q. Yin, G.-C. Guo, and Z.-F. Han, Temporal ghost imaging for quantum device evaluation, Opt. Lett. **44**, 2522 (2019).

[30] S. Fu, T. Wang, Z. Zhang, Y. Zhai, and C. Gao, Non-diffractive Bessel-Gauss beams for the detection of rotating object free of obstructions, Opt. Express **25**, 20098 (2017).

[31] D. B. Phillips, M. P. Lee, F. C. Speirits, S. M. Barnett, S. H. Simpson, M. P. J. Lavery, M. J. Padgett, and G. M. Gibson, Rotational Doppler velocimetry to probe the angular velocity of spinning microparticles, Phys. Rev. A **90**, 011801(R) (2014).

[32] H. Zhou, D. Fu, J. Dong, P. Zhang, and X. Zhang, Theoretical analysis and experimental verification on optical rotational Doppler effect, Opt. Express **24**, 10050 (2016).

[33] P. Llull, X. Liao, X. Yuan, J. Yang, D. Kittle, L. Carin, G. Sapiro, and D. J. Brady, Coded aperture compressive temporal imaging, Opt. Express **21**, 10526 (2013).

[34] M. P. Edgar, G. M. Gibson, and M. J. Padgett, Principles and prospects for single-pixel imaging, Nat. Photon. **13**, 13 (2019).

[35] Y. Bromberg, O. Katz, and Y. Silberberg, Ghost imaging with a single detector, Phys. Rev. A **79**, 053840 (2009).

[36] L. Hong, F. Lin, X. Qiu, and L. Chen, Second harmonic generation based joint transform correlator for human face

and QR code recognitions, Appl. Phys. Lett. **116**, 231101 (2020).

[37] M. P. J. Lavery, G. C. G. Berkhout, J. Courtial, and M. J. Padgett, Measurement of the light orbital angular momentum spectrum using an optical geometric transformation, J. Opt. **13**, 064006 (2011).

[38] O. Alan and W. Alan, *Signals and Systems* (Prentice-Hall Inc, New Jersey, 1997).

[39] B. I. Erkmen and J. H. Shapiro, Ghost imaging: From quantum to classical to computational, Adv. Opt. Photon. **2**, 405 (2010).

[40] J. H. Shapiro and R. W. Boyd, The physics of ghost imaging, Quantum Inf. Process. **11**, 949 (2012).

[41] M. J. Padgett and R. W. Boyd, An introduction to ghost imaging: Quantum and classical, Philos. Philos. Trans. R. Soc. A: Math., Phys. Eng. Sci. **375**, 20160233 (2017).